FULL PAPER

Magnetic Targeting Enhanced Theranostic Strategy Based on Multimodal Imaging for Selective Ablation of Cancer

*Zhiwei Li, Shengnan Yin, Liang Cheng, Kai Yang, Yonggang Li, and Zhuang Liu**

The booming development of nanomedicine offers great opportunities for cancer diagnostics and therapeutics. Herein, a magnetic targeting-enhanced cancer theranostic strategy using a multifunctional magnetic-plasmonic nano-agent is developed, and a highly effective in vivo tumor photothermal therapy, which is carefully planed based on magnetic resonance (MR)/photoacoustic (PA) multimodal imaging, is realized. By applying an external magnetic field (MF) focused on the targeted tumor, a magnetic targeting mediated enhanced permeability and retention (MT-EPR) effect is observed. While MR scanning provides tumor localization and reveals time-dependent tumor homing of nanoparticles for therapeutic planning, photoacoustic imaging with higher spatial resolution allows noninvasive fine tumor margin delineation and vivid visualization of three dimensional distributions of theranostic nanoparticles inside the tumor. Utilizing the near-infrared (NIR) plasmonic absorbance of those nanoparticles, selective photothermal tumor ablation, whose efficacy is predicted by real-time infrared thermal imaging intra-therapeutically, is carried out and then monitored by MR imaging for post-treatment prognosis. Overall, this study illustrates the concept of imaging-guided MF-targeted photothermal therapy based on a multifunctional nano-agent, aiming at optimizing therapeutic planning to achieve the most efficient cancer therapy.

1. Introduction

As the field of nanomedicine has emerged from the blending of nanoscience and biomedicine, theranostics with concurrent and complementary diagnostic and therapeutic capabilities based on nanotechnology offers great opportunities in the fight against cancer.[1] In an effort to realize the theranostic concept, the nano-platform should be deliberately engineered to simultaneously fulfill a number of features, including specific delivery of the theranostic agent to targeted lesions such as tumors, multimodal imaging contrasts to offer detailed tumor characteristics and enable post-therapeutic reexaminations under imaging techniques, highly efficient and controllable tumor therapy, as well as the satisfactory biosafety of the nano-agent.

The efficient delivery and specific targeting of theranostic agents to the tumor region are utmost important in cancer treatment.[2] A great deal of efforts has been paid to exploit various strategies to deliver theranostic agents to tumors with high efficiency and specificity. For example, the enhanced permeability and retention effect (EPR) of cancerous tumors could allow passive tumor accumulation of nanoparticles with appropriate sizes and surface coatings.[3] However, such a passive tumor targeting strategy suffers from the pathophysiological heterogeneity of tumors.[4] Molecular targeting is another well-established method relying the specific binding between targeting ligands conjugated on the nanoparticle surface and receptors over-expressed on the membrane of tumor cells or tumor vasculature cells. Unfortunately, despite the tremendous successes of molecular tumor targeting in many pre-clinical tumor models, its efficiency in real clinical cases has been largely limited by the significant inter-patient variations of receptor expressions.[5] In recent years, a number of other tumor targeting approaches utilizing physical forces or stimulus, such as magnetic field (MF), light, and ultra-sound, to enable tumor specific delivery of therapeutic agents have received significant interests,[6,7] as physical interactions are independent of the complicated cancer molecular biology pathways and their effects are more controllable and predictable. Among them, magnetic tumor targeting which uses magnetic nanoparticles carrying therapeutic functions and an external magnetic field focused on the targeted tumor region, has emerged as a promising approach that greatly overcomes limitations of molecular tumor targeting without being constrained by the specific receptor expression.[6,8]

In this work, we design a magnetic targeting enhanced theranostic strategy based on MR/PA multimodal imaging for selective photothermal ablation of tumors using gold shelled iron oxide nanoclusters with polyethylene glycol coating (IONC@Au-PEG). Such composite nanoparticles exhibit strong magnetic property and high near-infrared (NIR) optical absorbance,

Z. W. Li, Dr. L. Cheng, K. Yang, Prof. Z. Liu
Institute of Functional Nano & Soft Materials (FUNSOM)
Soochow University
Suzhou, 215123, China
E-mail: zliu@suda.edu.cn
Z. W. Li, Dr. L. Cheng, K. Yang, Prof. Z. Liu
Collaborative Innovation Center of Suzhou Nano Science and Technology
Soochow University
Suzhou, 215123, China
S. N. Yin, Dr. Y. G. Li
Department of Radiology
The First Affiliated Hospital of Soochow University
Suzhou, Jiangsu, 215006, China

DOI: 10.1002/adfm.201303345

and thus offer great contrasts in both magnetic resonance (MR) imaging, a traditional imaging approach widely used in the clinic for whole-body imaging,[9] and photoacoustic (PA) imaging, a recently emerged technique that allows higher-resolution imaging within a depth of a few cm.[10–12] In our study, both MR and PA imaging are carried out, not only to visualize the tumor, but also to determine the efficiency of magnetic tumor-targeting in a time-dependent manner for better therapeutic planning. Owing to the strong magnetism of theranostic nanoparticles, remarkably improved tumor homing of those nanoparticles is observed under magnetic targeting, likely owing to the "magnetic targeting mediated EPR effect". Photothermal treatment of cancer is then carefully planned and carried out. By finally tuning the laser power density and closely monitoring the tumor temperature, selective ablation of tumors under magnetic targeting is demonstrated. Moreover, at the post-treatment stage, imaging is further performed for tumor prognosis to evaluate the therapeutic outcome (**Figure 1**). Our work deliberately demonstrates the unique advantages of multimodal imaging guided therapeutic planning and post-treatment monitoring based on multifunctional theranostic nano-agents.

2. Results and discussion

The fabrication of IONC@Au and the subsequent functionalization with polyethylene glycol (PEG) was illustrated in **Figure 2**a. IONCs were synthesized using a binary solvent thermal method according to the literature protocol with slight modifications.[13] Being clusters of nanocrystals (Supporting Information, Figure S1), the as-made IONCs showed rather uniform sizes with an average diameter of ≈100 nm (Figure 2b,c and Supporting Information, Figure S2a). Dopamine (DA) was introduced to modify IONCs,[14] making those nano-clusters water-soluble and positively charged with a zeta potential of +19 mV (Supporting Information, Figure S2b), which facilitated the adsorption of negative-charged gold seeds through the electrostatic interaction.[15] Afterwards, an in-suit seed-mediated gold growth was carried out by reduction of $HAuCl_4$ to form a dense gold shell outside IONCs.[16] Transmission electron microscopy (TEM) images of nano-clusters before and after gold growth witnessed the formation of a dense gold shell with seeds (small dark dots) embedded on top of IONCs. The core/shell multi-component structure of IONC@Au was further confirmed by the high-angle annular dark field scanning TEM (HAADF-STEM) images (Figure 2d) and energy-dispersive X-ray spectroscopy (EDS) (Figure 2e), both of which revealed the uniform coating of Au on IONCs. After the growth of gold shell, the obtained IONC@Au was then modified by lipoic acid terminated PEG (LA-PEG, 5 kDa) through the gold-thiol bond. The successful PEGylation was evidenced by the infrared (IR) spectra as well as the remarkably enhanced physiological stability of IONC@Au-PEG (Supporting Information, Figure S3a,b).

By adjusting the added volume of gold growth solution, the gold shell thickness as well as the absorbance of IONC@Au-PEG composites could be controlled. UV/Vis/NIR spectra of IONC@Au-PEG after adding different volumes of the growth solution showed the enhanced NIR absorbance of the sample as the volume increase of $HAuCl_4$ growth solution from 5 mL to 50 mL (Figure 2f), consistent to the increased gold shell thickness as revealed by TEM images (Supporting Information, Figure S4). However, further increase of $HAuCl_4$ volume from 50 mL to 100 mL resulted in obvious aggregation of composite nanoparticles (Supporting Information, Figure S4), and offered little additional enhancement of NIR absorbance. Consequently, we chose the sample prepared by adding 50 mL of growth solution (the optimized synthesis condition) for the previous materials characterization (Figure 2b-e, Supporting Information, Figures S2,S3) and the followed experiments. The precise molar ratio of Fe_3O_4/Au in this nanocomposite was measured to be 2.55:1 by inductively coupled plasma atomic emission spectroscopy (ICP-AES).

Next, the magnetic properties of IONCs and IONC@Au-PEG were studied. The field-dependent magnetization measurement suggested the superparamagnetic nature of IONCs before and after gold coating (Figure 2g). While being well dispersed in water without any aggregation, IONC@Au-PEG once exposed to an external magnetic field could be rapidly attracted by the magnet (Figure 2g, inset). With a concentration-dependent darkening effect in T2-weighted MR images, the T2 relaxivity of IONC@Au-PEG was determined to

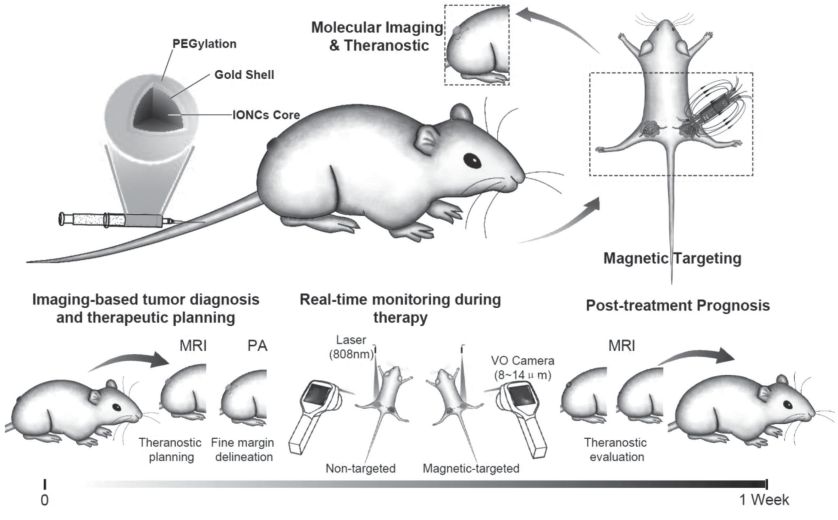

Figure 1. The magnetic targeting enhanced theranostic strategy using IONC@Au-PEG nanoparticles under guidance by multimodal imaging. In our experiment, IONC@Au-PEG is intravenously injected into a mouse bearing two tumors, one of which is exposed to an external magnetic field while the other is not. As the theranostic nanoparticles circulate in bloodstream, they will be trapped into the magnetic field created by the nearby magnet, resulting in enhanced enrichment and prolonged retention in the targeted tumor. Dual modal MR and photoacoustic imaging is carried out to track and understand the tumor homing of our theranostic nanoparticles for therapeutic planning. IR thermal imaging is conducted during NIR laser irradiation to real-time monitor the photothermal effect for better therapeutic control. MR imaging after photothermal therapy is finally performed for post-treatment prognosis.

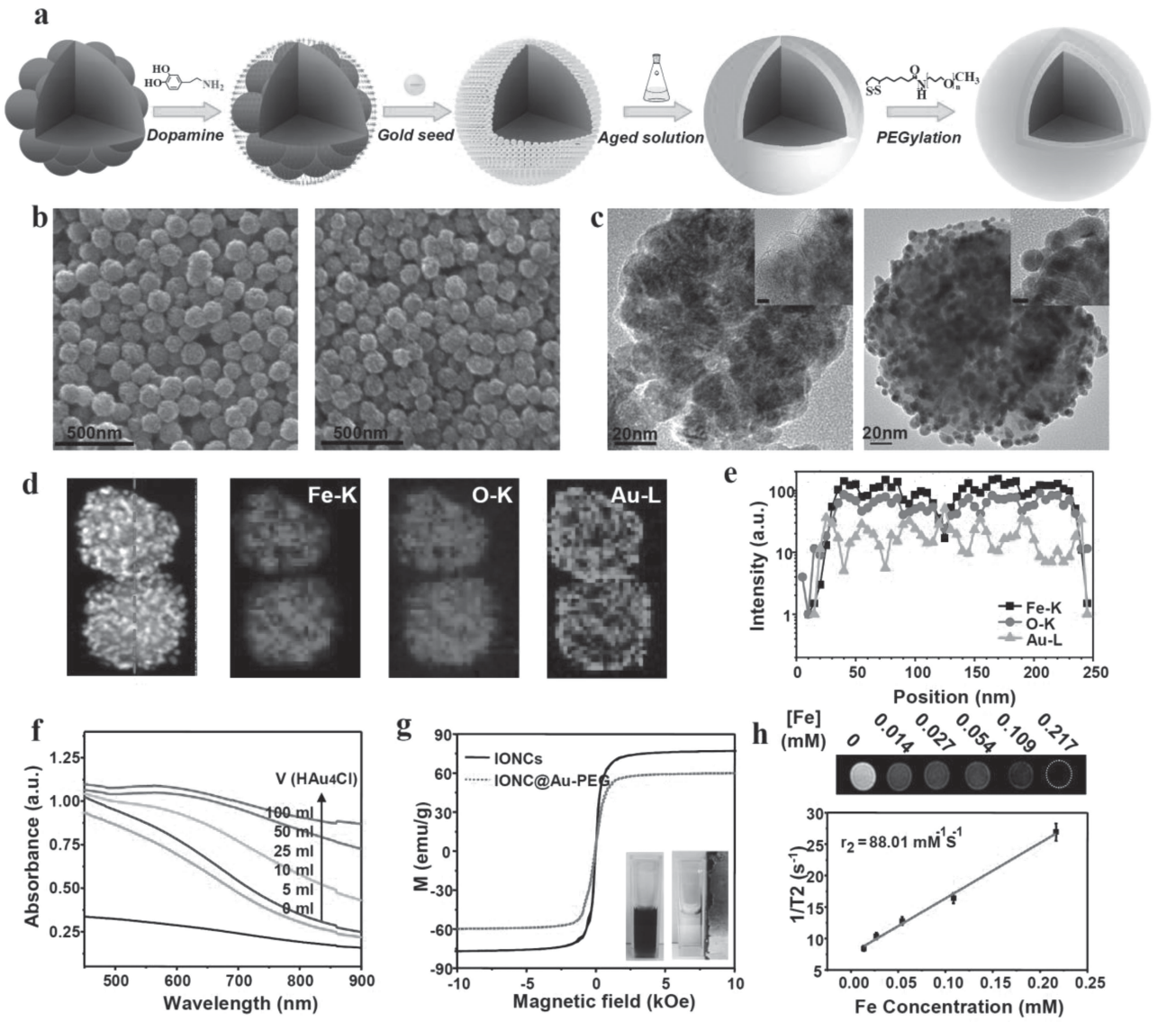

Figure 2. Preparation and characterization of IONC@Au-PEG. a) A simplified procedure for the fabrication of IONC@Au-PEG theranostic nanoparticles. b) SEM images of IONCs (left) and IONC@Au-PEG (right). c) TEM images of IONCs (left) and IONC@Au-PEG (right). d) STEM image and HAADF-STEM-EDS mapping images of IONC@Au-PEG. e) Cross-sectional compositional line profile in STEM pattern highlighted in (d). f) UV-Vis-NIR spectra of IONC@Au-PEG prepared by adding different volumes of gold growth solution. g) Magnetization loops of IONCs and IONC@Au-PEG. Inset: photos of IONC@Au-PEG aqueous solution without (left) and with (right) exposure to an external magnetic field. h) The T2-weighted MR images of IONC@Au-PEG under various Fe concentration and the relative relaxation rate R2.

be 88.01 mM^{-1} S^{-1} (in H_2O at a field strength of 3 T at room temperature) (Figure 2h), suggesting the feasibility of using our composite nanoparticles as a contrast agent in MR imaging.

The bio-compatibility and safety of nano-agents are one of the main concerns in the area of nanomedicine. As ferrite nanoparticles could gradually decomposed into iron ions and several formulations of functionalized iron oxide nanoparticles have already been used for clinical MR diagnosis for many years, they have been proven to be biocompatible after administration.[17] Besides, it has been evidenced that the chemical inertness nature of gold nanomaterials renders them low toxicity in biological systems.[18,19] As for PEGylated IONC@Au core/shell nanocomposite developed in this work, their in vitro cytotoxicity was firstly determined by the standard methyl thiazolyl tetrazolium (MTT) cell viability assay (**Figure 3**a), which indicated no obvious cytotoxicity with the nanoparticle concentration increased up to 0.4 mg/mL. Furthermore, lactate dehydrogenase (LDH) leakage and intracellular reactive oxygen species (ROS) generation were examined to evaluate the possible cell membrane damage and oxidative stress of cells induced by IONC@Au-PEG, respectively. Our data revealed that those nanoparticles even at the highest tested concentration resulted in neither appreciable LDH leakage nor oxidative stress to cells (Figure 3b).

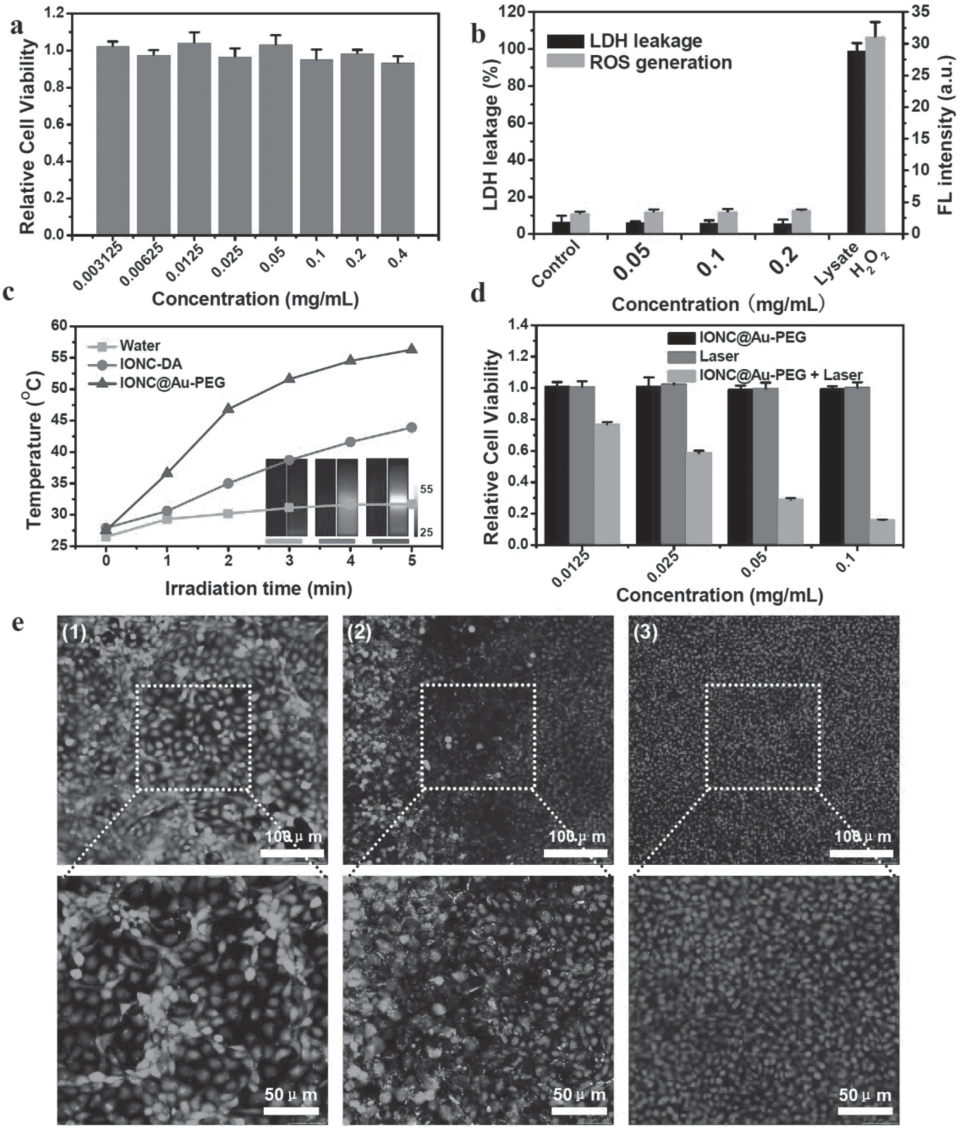

Figure 3. In vitro experiments. a) Relative cell viability data determined by the MTT assay after culturing 4T1 cells with IONC@Au-PEG at various concentrations for 24 h. b) Data of LDH leakage and ROS generation assays of cells after incubation with IONC@Au-PEG under various concentrations for 24 h. Triton X-100 and H_2O_2 were added as the positive controls for LDH and ROS assays, respectively. c) Photothermal heating curves of water, IONCs and IONC@Au-PEG under laser irradiation (808 nm, 1 W cm^{-2}, 5 min). Inset: IR thermal imaging of water (left), IONCs (middle) and IONC@Au-PEG (right) solutions before and after laser irradiation. d) The concentration-dependent in vitro photothermal therapy after laser irradiation (808 nm, 1 W cm^{-2}, 5 min). The relative cell viabilities after various treatments were determined by the MTT assay. e) Confocal fluorescence images of Calcein AM and PI co-stained 4T1 cells after MF-targeted in vitro photothermal therapy irradiated by a laser (808 nm, 1 W cm^{-2}, 5 min). Images were taken at different locations in the culture dish: 1) far from the magnet, 2) in the middle, and 3) nearby the magnet.

Next, we tested the photothermal performance of IONC@Au-PEG nanoparticles under NIR laser exposure. Owing to the high NIR absorbance, an aqueous solution of IONC@Au-PEG (1 mg mL^{-1}) could be rapidly heated up to ≈57 °C after being irradiated by an 808-nm laser under a power density of 1 W cm^{-2} for 5 min (Figure 3c). In contrast, IONCs without gold coating showed much less effective photothermal heating because of their low absorbance at 808 nm. The photothermal effect induced tumor cell death was then demonstrated with 4T1 cells. As expected, nanoparticle concentration-dependent photothermal destruction of cancer cells was observed, with the majority of cells killed after incubation with 0.1 mg mL^{-1} of IONC@Au-PEG and exposed to the 808-nm laser at 1 W cm^{-2} for 5 min (Figure 3d). To demonstrate the in vitro magnetic field (MF) controlled photothermal cancer ablation, 4T1 cells were incubated with IONC@Au-PEG in a cell culture dish, beneath which a magnet was placed. Owing to the localized accumulation of IONC@Au-PEG nanoparticles induced by the MF, only those cells nearby the magnet were effective ablated by the NIR laser (808 nm, 1 W cm^{-2}, 5 min), leaving the rest cells untouched (Figure 3e).

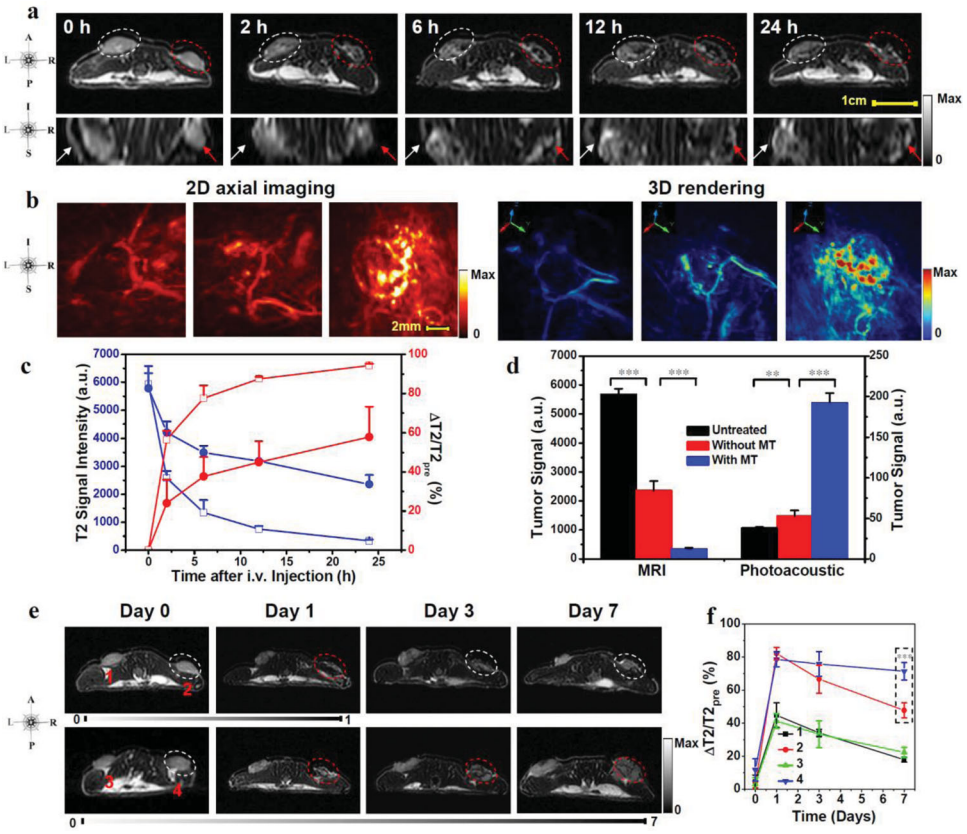

Figure 4. In vivo MR/photoacoustic dual-modal imaging. a) T2-weighted in vivo MR images acquired at different time intervals post injection of IONC@Au-PEG. A much more remarkable time-dependent darkening effect in MF-targeted tumor (on the right) than that in the non-targeted (on the left) was observed. b) 2D and 3D photoacoustic imaging of tumors taken 24 hours after injection of IONC@Au-PEG. From left to right: PA imaging of control, non-targeted and MF-targeted tumor. c) T2 signal intensities and relative T2-signal change (△T2/T2%) of tumors at different time intervals post injection. d) Quantification of MR and photoacoustic signals in tumors 24 hours post injection of IONC@Au-PEG. e) Study of long-term tumor retention of IONC@Au-PEG under magnetic targeting for 1 day (upper) or 7 days (lower) by MR imaging. White and red dashed circles indicate tumors in the absence and presence of magnetic targeting, respectively. f) The quantitative T2 signal changes at different time intervals corresponding to images in (e). P values were calculated by student's t-test: $***P < 0.001$, $**P < 0.01$.

We then wondered whether the external magnetic field would guide the tumor specific homing of PEGylated IONC@Au nanoparticles. Balb/c mice each bearing two 4T1 tumors were intravenously (i.v.) injected with IONC@Au-PEG (200 µL, 2 mg mL^{-1}) through the tail vein. To enable magnetic targeting, a magnet was securely attached onto the right tumor of each mouse by a bandage all the time in our experiments except being shortly taken off during imaging. Those mice were then imaged by a 3 T MR scanner at various time intervals post injection (p.i.) (**Figure 4**a). Both MF-targeted and non-targeted tumors showed obvious time-dependent darkening effects in T2-weighted MR images post injection of IONC@Au-PEG, indicating the passive tumor accumulation of nanoparticles as a result of the tumor EPR effect. Notably, compared to the non-targeted tumors (white dashed circles and arrows), the MF-targeted tumors (red dashed circles & arrows) appeared to be much darker in T2-MR images, highlighting the remarkably enhanced tumor homing of our theranostic nanoparticles under magnetic targeting.

Photoacoustic imaging is able to detect ultrasound waves generated from thermally induced expansion and vibration of light absorbing tissues under pulsed laser irradiation.[12] While MR imaging is capable of whole-body imaging without any depth limit,[20] photoacoustic imaging offers much higher spatial resolution and could image tissues in a localized region with a maximal depth of 5–7 cm.[11,21] Thus, in our study, PA imaging was carried out, in order to allow fine margin delineation of the tumor, visualize the tumor micro-structures (e.g., vasculature structures), and understand the intratumor distribution of IONC@Au-PEG nanoparticles at a higher spatial resolution (Figure 4b,c). While both 2D and 3D rendering of PA images revealed the major vasculatures in the tumor of a mouse prior to the injection of nanoparticles, strong PA signals which were mainly associated with the tumor vasculatures were observed in the MF-targeted tumor of this mouse 24 h after injection with IONC@Au-PEG. The non-targeted tumor, on the other hand, showed much weaker PA signals, consistent to the MR imaging data. Therefore, we could conclude that the external MF is able to attract IONC@Au-PEG magnetic nanoparticles circulating in the blood vessels to the tumor region, where the vasculatures are disordered and damaged, leading

to the increased tumor accumulation of those nanoparticles by enhancing the intrinsic EPR effect of the tumor. Such phenomenon may be named as the 'magnetic targeting-enhanced EPR' (MT-EPR) effect.

Both MR and PA imaging results were then quantitatively analyzed using the region-of-interest (ROI) quantification. The in vivo tumor-homing kinetics of IONC@Au-PEG was studied based on MR imaging data of T2 signals in the tumors. As shown in Figure 4c, T2 signals in two groups of tumors were both obviously decreased after injection of IONC@Au-PEG, with sharp declines noticed within the first 6 h post injection. Notably, T2 signals in MF-targeted tumors decreased more remarkably than that in non-targeted tumors due to the enhanced enrichment of magnetic theranostic nanoparticles under the applied external MF. At 24 h p.i., the MR T2 signals decreased by 94.1% in MF-targeted tumors, compared with 58.5% of signal decrease in non-targeted tumors ($P = 0.0005$), whereas the photoacoustic signals increased 1.4 folds and 5.1 folds in non-targeted and MF-targeted tumors, respectively (Figure 4d).

To confirm the imaging results, the in vivo blood circulation and biodistribution of IONC@Au-PEG were examined after i.v. injection by measuring the Au^{3+} levels in various organs or blood samples using ICP-AES. The Au^{3+} levels in blood decayed in accordance with a two-compartment model with first ($t_{1/2}$) and second ($t'_{1/2}$) phase of circulation half-lives calculated to be 0.37 ± 0.05 h and 4.78 ± 0.50 h, respectively (Supporting Information, Figure S6a). Biodistribution data of IONC@Au-PEG based on Au^{3+} levels at 24 h p.i. showed high accumulation of nanoparticles in the reticuloendothelial system (RES) including liver and spleen, as well as the effective tumor homing of nanoparticles under magnetic targeting, with the uptake level of IONC@Au-PEG in the MF-targeted tumor measured to be 15.5 ± 1.7%ID g^{-1}, which was nearly 3 folds higher than that in non-targeted tumors. Consistent to biodistribution data, Prussian blue stained images of various organs also illustrated the significant accumulation of our nanoparticles in the liver, spleen, and MF-targeted tumor.

In addition, the long-term in vivo kinetics of nanoparticles was further studied by MR imaging to investigate the influence of magnetic targeting on the retention performance of IONC@Au-PEG in the solid tumor. The relative T2 signal change ($\Delta T2/T2_{pre}$), an indicator of nanoparticle retention in the tumor, decreased dramatically within 7 days once the magnetic targeting stopped at 1 day p.i. This was likely due to the translocation and clearance of IONC@Au-PEG by the lymphatic circulation,[22] and the dilution of nanoparticles by the increased tumor volume. Interestingly, for tumors continuously attached to the magnet for 7 days, the MR contrast remained almost constant (Figure 4e,f). Therefore, magnetic targeting can remarkably enhance the retention of magnetic theranostic agents in the MF-targeted tumor, as a result of MT-EPR effect. Compared with the native EPR effect of cancerous tumors with disordered blood vessels and impoverished lymphatic system,[23] such MT-EPR effect allows for controllable tumor targeting and retention utilizing the magnetic force.

Considering the imaging data that the MR contrast in the tumor approached the highest level at 24 h p.i. and remained unchanged afterwards, we thus conducted in vivo photothermal therapy of cancer at 24 h after i.v. injection of IONC@Au-PEG (200 μL, 2 mg mL^{-1}) under magnetic tumor targeting. The detailed theranostic schedule is presented in **Figure 5**a. Based on the obtained imaging information right after injection of our theranostic agent, photothermal therapy was triggered by laser irradiation at day 1, accompanied by real time infrared thermal imaging. Afterwards, the therapeutic outcome was evaluated by the followed MR imaging, and confirmed by the measurement of tumor volumes.

For intra-therapeutic monitoring the temperature changes in real time, infrared thermal imaging was introduced during the 808-nm NIR laser irradiation at different powder densities (0.5 W cm^{-2}, 0.8 W cm^{-2}, or 1 W cm^{-2}) (Figure 5b). Due to the laser power dependence of photothermal effect in photothermal therapy, it is vital to optimize laser power density to achieve satisfactory therapeutic efficacy and meanwhile minimize thermal damage to the surrounding normal tissues.[24] In our experiments, we found that the photothermal effect at the power density of 0.5 W cm^{-2} was not sufficient for tumor ablation as the local temperature increase was neglectable for the non-targeted tumor and less than 10 °C even for the MF-targeted tumor (Figure 5c). Since under such conditions the maximum tumor temperature was far below 45 °C,[25] which was usually regarded as the minimal threshold of hyperthermia therapy, no appreciable tumor damage was noticed after laser irradiation. We then increased the laser power density to 0.8 and 1.0 W cm^{-2} and monitored the tumor temperatures under NIR laser irradiations. As for 0.8 W cm^{-2}, the maximum temperature in the MF-targeted tumor rapidly increased from 35 °C to 53 °C whereas the non-targeted tumors only showed a ≈10 °C increase with maximum temperature to be ≈44.5 °C after laser irradiation (Figure 5d). As the result, the MF-targeted tumor was completed ablated leaving a black scar at the original tumor site one day after irradiation, while the non-targeted tumor was not significantly affected. When the laser power density reached to 1.0 W cm^{-2}, the local temperatures in both MF-targeted and non-targeted tumors increased to be above 45 °C after a short period of laser exposure, leading to the ablation of both tumors (Figure 5e). Therefore, real-time monitoring of tumor temperature is obviously critical to determine the therapeutic outcome of photothermal therapy. In our system, considering the effectively tumor-homing of our theranostic nano-agent under magnetic targeting, the laser power density at 0.8 W cm^{-2} could be optimal to selectively burn the MF-targeted tumor and induce the minimal damage to the surrounding normal tissues.

Similar to various literatures reported previously,[26] a scar formed in most situations where the original tumor was eliminated one day after laser irradiation (Figure 5d), making it difficult to evaluate whether the deeper tumor tissue was completely ablated or not at the early stage post treatment. Furthermore, as for other tumor models inside the living body instead of subcutaneous model, reliable imaging techniques are also required to record the post-therapeutic proliferation of tumors to understand the tumor therapeutic response. To fulfill such requirement, we thus used MR imaging with unlimited tissue penetration to assess the therapeutic outcome after photothermal treatment of tumors on mice. As shown in Figure 5f, T2-weighted MR images clearly revealed the elimination of MF-targeted tumor after laser irradiation (808-nm, 0.8 W cm^{-2},

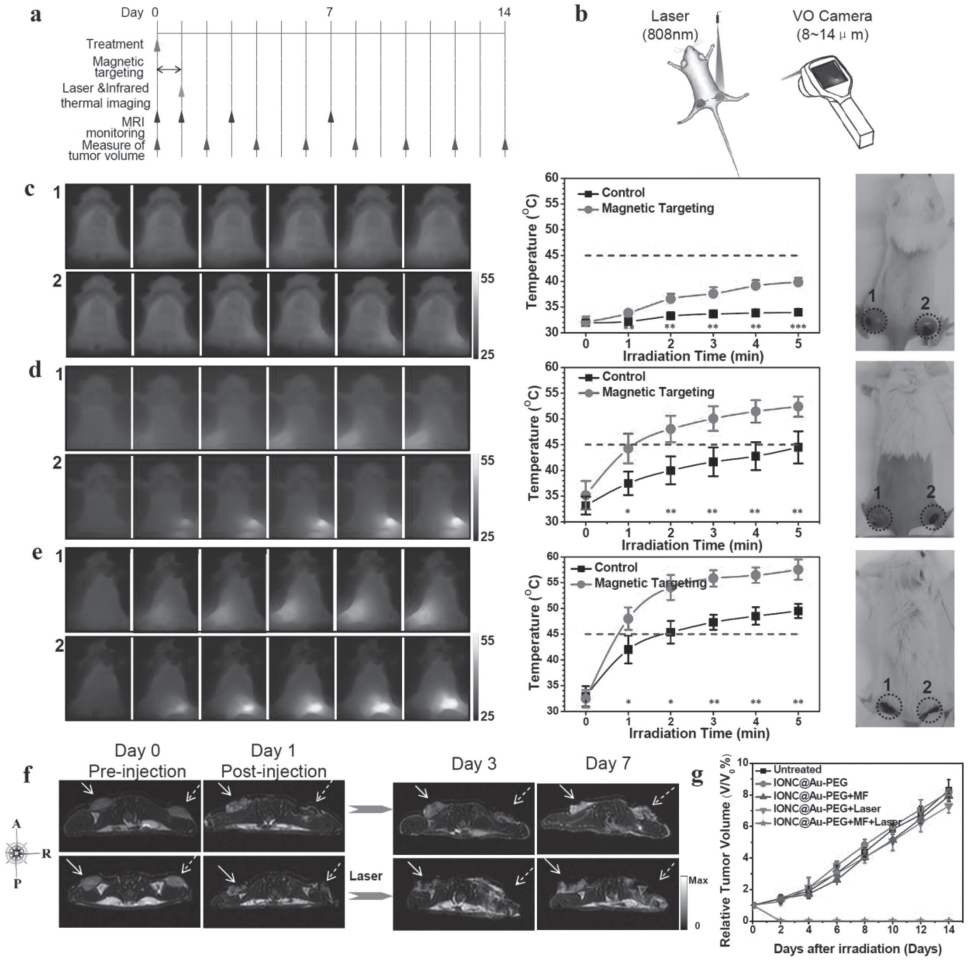

Figure 5. Magnetic targeting enhanced in vivo photothermal therapy. a) The theranostic schedule for imaging-guided photothermal ablation of cancer. b) Schematic illustration of the infrared thermal imaging to real time monitor the temperature changes intra-therapeutically. c–e) Real time in vivo IR thermal imaging and tumor temperature rise curves of mice during laser irradiation at 808 nm under different power densities at c) 0.5 W cm^{-2}, d) 0.8 W cm^{-2}, and e) 1 W cm^{-2} for 5 min. Tumors on the right side (2) were exposed to an external MF for 1 day while those on the left side (1) were not. The photos shown on the right side were mice 1 day after laser irradiations. f) MR images of IONC@Au-PEG injected 4T1 tumor-bearing mice without (up) and with (bottom) laser irradiation (808 nm, 0.8 W cm^{-2}, 5 min). The solid and dashed arrows indicate non-targeted and MF-targeted tumors, respectively. g) Tumor growth curves of mice after different treatment processes as indicated. *P* values: ***$P < 0.001$, **$P < 0.01$, *$P < 0.05$.

5 min) without any deep tumor residue remaining or tumor regrowth during a week. Although the non-targeted tumor was also partly damaged after laser irradiation at the same condition, a large portion of the tumor mass underneath the skin survived during photothermal treatment and maintained its normal growth. We then tracked the tumor growth by measuring the tumor volumes post various treatments by a caliper (Figure 5g). MF-targeted tumors after laser irradiation were completely eliminated without regrowth during two weeks. To the contrary, the growth of non-targeted tumors was not significantly delayed, although their temperatures showed a moderate increase during laser irradiation. Injection of IONC@Au-PEG particles but without laser irradiation, regardless of the exposure to the magnetic field, showed no effect to the tumor growth.

Previous studies have demonstrated that gold and ferrite nanomaterials with appropriate surface coatings are usually non-toxic in biological systems.[19,24] During our experiment, no obvious body weight loss was observed after various treatments (Supporting Information, Figure S7). To investigate the potential long-term in vivo cytotoxicity of our theranostic nanoparticles, healthy mice were i.v. injected with IONC@Au-PEG (200 μL, 2 mg mL^{-1}) and closely monitored for 30 days. Major organs were collected for histological examination by hematoxylin and eosin (H&E) staining, which revealed no noticeable organ damage or inflammatory lesion (Supporting Information, Figure S8). Therefore, our preliminary study showed no obvious toxic side effects to mice at the tested dosage of IONC@Au-PEG.

3. Conclusion

Briefly, we have designed a magnetic targeting enhanced cancer theranostic strategy which is guided by MR/photoacoustic dual-modal imaging using IONC@Au-PEG as a

promising theranostic agent. While whole-body MR imaging is able to determine the overall uptake level of magnetic nanoparticle in the tumor, PA imaging could vividly illustrate the heterogeneous intratumoral distribution of nanoparticles,[27] beneficial not only for understanding the tumor homing mechanism of those theranostic nanoparticles, but also for better planning of therapies to achieve the optimized treatment efficacy. Replying on those imaging approaches, we found that magnetic targeting by attaching a magnet nearby the tumor would remarkably enhance the tumor homing and retention of our magnetic theranostic nanoparticles, owing a so called MT-EPR effect. More importantly, the enhanced enrichment of IONC@Au-PEG through magnetic targeting allows us to photothermally ablate tumors under a mild power density at 0.8 W cm^{-2}, which is the optimized power density based on real-time IR thermal imaging and lower than that normally needed using gold nanomaterials with different morphologies as the photothermal agent for in vivo cancer ablation therapy (1–4 W cm^{-2}).[24,28]

Overall, our study strategy achieves: I) magnetic targeting enhanced EPR effect of magnetic theranostic agent specifically in the targeted tumor; II) whole-body tumor localization/imaging by MR imaging and high-resolution 3D visualization of theranostic agents within the tumor for better pre-therapeutic planning; III) visualized therapeutic procedure using IR thermal imaging for selective and controllable photothermal tumor ablation; IV) a reliable approach by post-therapeutic imaging to determine the therapeutic outcomes. Therefore, the magnetic targeting enhanced theranostic strategy described here could potentially enable highly effective tumor ablation therapy that could be carefully planned before treatment, precisely controlled during treatment, and with accurate prognosis after treatment.

4. Experimental Section

4.1. Materials

Ferric chloride hexahydrate (FeCl3·6H2O), sodium acetate (CH3COONa, NaOAc), ethanol, ethylene glycol (EG), diethylene glycol (DEG) and polyvinylpyrrolidone (PVP, K-30) were purchased from Sinopharm Chemical Reagent Co., Ltd. Dopamine (DA) and lipoic acid (LA) were obtained from Sigma-Aldrich. Amino group terminated poly ethylene glycol (PEG-NH_2, 5K) was purchased from Aladdin.

4.2. Synthesis of IONC-DA

Preparation of IONCs: IONCs were synthesized using a solvent thermal method according to literature with a little modification. Generally, $FeCl_3{\cdot}6H_2O$ was dissolved in EG (6 mL) and DEG (14 mL), stirring for 30min at room temperature. Then, 2 g PVP were added into the above solution and heated to 125 °C for 1 h. 1.5 g of NaOAc were added after the heating was stopped. Reacting for another 0.5 h, the mixture was transferred to a Teflon-lined stainless-steel autoclave (20 mL), which was heated at 200 °C for 12 h afterwards. The obtained IONCs were washed by a mixture of water and ethanol three times and re-dispersed in tetrahydrofuran (THF).

DA Modification: 20 mg DA dissolved in 2 mL water were added into 5 mL THF containing 20 mg IONCs. After being sonicated for 1 h, the mixture was stirred at room temperature overnight. The excess DA was removed by magnetic separation. The obtained IONC-DA was dispersed in 20 mL water.

4.3. Preparation of LA-PEG

The synthesis of LA-PEG was conducted following a literature protocol. Generally, 500 mg mPEG-NH_2 (5K) were reacted with 41.3 mg lipoic acid (LA) (mPEG: LA molar ratio = 1:2) in 2 mL dichloromethane for 2 days at the presence of 62 mg *N*,*N*'-dicyclohexylcarbodiimide (DCC, Sigma-Aldrich) and 56 µL triethylamine. After reaction, the solution was blown to dry by nitrogen. Water was then added with the solution pH adjusted to 11–12 by sodium hydroxide. Precipitation was removed by centrifugation (14800 rpm, 5 min) and filtration (0.22 µm). Filtrate solution was extracted by dichloromethane for three times. After evaporating the organic solution, the product was dispersed in water and then frozen-dried.

4.4. Fabrication of IONC@Au-PEG

Gold Seed: Typically, 12 µL tetrakis-hydroxymethyl-phosphonium chloride (THPC) and 250 mL NaOH (2 M) were added into 45 mL deionized water sequentially. After stirring for 5 min, 2 mL $HAuCl_4$ (1%) were added into the above solution, which was then stirred in dark overnight.

Growth Solution: 1.5 mL $HAuCl_4$ (1%) were added into 100 mL deionized water containing 25 mg potassium carbonate. 10 min later, the solution became coreless. The growth solution was aged for one day before use. The concentration of $HAuCl_4$ is about 0.44 µM.

Gold Seed Adsorption: The negative charged gold seeds could be absorbed onto the surface of positively charged IONC-DA by electrostatic interaction. 8 mL gold seed solution were added into 5 mL IONC-DA (1 mg mL^{-1}) aqueous solution. Acetic acid (0.2 M) was introduced to adjust the pH to ≈4.0. The mixture was shocked vigorously overnight and then the excess gold seeds were removed through magnetic separation twice, leaving the seeds attached on IONC-DA for further shell growth.

Gold Shell Growth: To form a dense gold shell, a seed-induced in-suit growth method was carried out. Various volumes (5–100 mL) of aged growth solution were added into 5 mL of IONC-DA (1 mg mL^{-1}) with gold seeds attached under vigorously stirring. Formaldehyde (29%) was introduced drop-wisely as the reducing agent. After reaction for 30 min, 10 mg LA-PEG was added into the solution. The prepared IONC@Au-PEG was purified through magnetic separation and the as-made nanoparticles were dispersed in 2.5 mL deionized water. The precious concentration was measured by inductively coupled plasma atomic emission spectrometry (ICP-AES).

4.5. Characterization

The size and morphology of as-made nanoparticles were characterized by scanning electron microscopy (SEM, FEI quanta 200F), transmission electron microscopy (TEM), and high-resolution TEM (HR-TEM, Philips CM300) under an accelerate voltage of 200 kV. UV/Vis/NIR spectra were carried out using PerkinElmer Lambda 750 UV/Vis/NIR spectrophotometer. IONC@Au-PEG was prepared under various concentrations (0–0.217 mM of Fe) and scanned under a 3.0-T clinical MRI scanner at room temperature. T2-weighted MR images were acquired using the following parameters: TR 2000 ms; TE 106.4 ms; slice thickness 1.0 mm; slice spacing, 0.2 mm; matrix, 224 × 192; FOV 10 cm × 10 cm. Afterwards, the T2 signal intensity was measured within a manually drawn region-of-interest (ROI) for each sample. Then, relaxation rate R2 was calculated as the reciprocal of T2. R2 coefficient was the slope of fitting linear of R2 as a function of Fe concentrations.

4.6. In Vitro Experiments

Murine breast 4T1 cancer cells originated from American Type Culture Collection (ATCC) were cultured in RPMI-1640 medium containing 10% FBS and 1% penicillin/streptomycin at 37 °C under 5% CO_2. Cell viabilities were measured using a standard methyl thiazolyltetrazolium (MTT, Sigma-Aldrich) assay.

Cell membrane integrity was determined by lactate dehydrogenase (LDH) leakage assay (Promega Cat. 7890) following the vendor's protocol. In the experiment, 4T1 cells lysed by the lysis solution were used as the positive control, while the cell-free mediums were used as the negative control. The analyses were performed with a microplate reader (Bio-Rad).

Intracellular ROS production was evaluated by a dihydroethidine (DHE) probe known to be oxidized by various oxidative agents. 4T1 cells were seeded into 6-well culture plates at 8×10^5 per well. After culturing with different concentrations of IONC@Au-PEG solution for 24 h, cells were washed and re-suspended in cell culture medium containing 1 μM DHE (sigma), and analyzed using a flow cytometry (FACS Calibur from Becton, Dickinson and Company).

As for in vitro PTT, 4T1 cells were cultured with IONC@Au-PEG under different concentrations. 24 h later, cells were exposed to laser (808 nm, 5 min). After another 12 h, cells viabilities were measured by MTT.

4T1 cells (1×10^5 cells) were cultured in a 35-mm culture dish containing 2 mL RPMI-1640 medium with a magnet placed beneath. 50 μL of 2 mg mL^{-1} IONC@Au-PEG was added. After incubation for 4 h, cells were exposed to laser (808 nm, 1 W cm^{-2}) for 5 min. After culturing for another 12 hours, dead and live cells were stained with propidium iodide (PI, 5 μM) and Calcein AM (2 μM), respectively. Fluorescence of 4T1 cells at different regions was imaged.

4.7. Tumor Model

Balb/c mice weighing ≈20 g were purchased from Suzhou Belda Bio-Pharmaceutical Co., Ltd. and used in accordance with regulations provided by Soochow University Laboratory Animal Center. 4T1 cells were inoculated by subcutaneous injection of 5×10^6 cells in ≈50 μL serum-free RMPI-1640 medium onto the back of female Balb/c mice. Each mouse was inoculated with two tumors on both sides. In vivo experiments were carried out when the tumor volume reached to ≈50 mm^3.

4.8. In Vivo MR/PA Duel-Modal Imaging Under Magnetic Targeting

Tumor-bearing mice were intravenously injected with 200 μL 2 mg mL^{-1} IONC@Au-PEG. Afterwards, tumor on the right was exposed to an external magnetic field (3000 Gs) for 1 day while the left was not. T2-weighted MR images were taken on a 3 T clinical MRI scanner (Bruker Biospin Corporation, Billerica, MA, USA) equipped with small animal imaging coil. T_2-weighted images were acquired using the following parameters: TR 2000 ms; TE 106.4 ms; slice thickness 2.0 mm; slice spacing, 0.2 mm; matrix, 224 × 192; FOV 10 cm × 10 cm. Photoacoustic (PA) imaging was carried out with the excitation wavelength at 700 nm using Endra Nexus 128 PA imaging system (Endra Inc., Michigan, USA) in the Center for Molecular Imaging and Translation Medicine, Xiamen University. Three-dimensional rendering of MRI and PA imaging was performed using the commercial soft ware, Osirix.

4.9. Blood Circulation and Biodistribution

Five healthy mice were i.v. injected with IONC@Au-PEG (200 μL, 2 mg mL^{-1}). About 10 μL blood was extracted from the tail vein at different time intervals. After being weighted, the blood was dissolved in aqua regia (6 mL HCl, 2 mL HNO_3 and 2 mL $HClO_4$) under 300 °C for ≈2 h. The obtained homogeneous solution was diluted to 10 mL with deionized water. The concentration of Au^{3+} was measured by ICP-AES.

Five tumor-bearing mice were sacrificed at 24 h after i.v. injection of IONC@Au-PEG (200 μL, 2 mg mL^{-1}) with magnetic targeting. Various organs were collected and solubilized by aqua regia. The enrichment of theranostic agents in each organ was analyzed using ICP-AES as described above.

4.10. In Vivo Magnetic Targeting and PTT

Mice inoculated with two tumors were i.v. injected with IONC@Au-PEG (200 μL, 2 mg mL^{-1}) when the size of tumors approached ≈50 mm^3. Tumors on the right were exposed to an external magnetic field (3000 Gs) immediately and continued for one day. For the laser treatment groups (six mice), both of the two tumors on each mouse were irradiated by an optical fiber coupled 808-nm NIR laser (Hi-Tech Optoelectronics Co, Ltd. Beijing, China) at the desired power density (0.5, 0.8, or 1.0 W cm^{-2}) for 5 min. The precise optical power was calibrated using an optical power meter (LPE-1C, Physcience Opto-Electronics, Beijing). During laser irradiation, infrared thermal imaging was conducted simultaneously to monitor the photon-thermal transformation efficiency. As control groups, six mice without laser irradiation and six untreated mice were introduced. Tumor size was measured every two days and calculated by (length of tumor) × (width of tumor)^2/2.

Acknowledgements

This work was partially supported by the National Natural Science Foundation of China (51222203, 51302180), the National "973" Program of China (2011CB911002, 2012CB932601), and a Project Funded by the Priority Academic Program Development of Jiangsu Higher Education Institutions. Dr. Liang Cheng was supported by a Post-doctoral research program of Jiangsu Province (1202044C) and a Post-doctoral science foundation of China (2013M531400). The authors thank Prof. Gang Liu in the Center for Molecular Imaging and Translational Medicine at Xiamen University for his great help in photoacoustic imaging.

Received: September 28, 2013
Revised: October 28, 2013
Published online: December 5, 2013

[1] a) J. V. Jokerst, S. S. Gambhir, *Acc. Chem. Res.* **2011**, *44*, 1050; b) W. Dong, Y. Li, D. Niu, Z. Ma, J. Gu, Y. Chen, W. Zhao, X. Liu, C. Liu, J. Shi, *Adv. Mater.* **2011**, *23*, 5392.
[2] K. Kim, J. H. Kim, H. Park, Y.-S. Kim, K. Park, H. Nam, S. Lee, J. H. Park, R.-W. Park, I.-S. Kim, *J. Controlled Release* **2010**, *146*, 219.
[3] A. K. Iyer, G. Khaled, J. Fang, H. Maeda, *Drug Discovery Today* **2006**, *11*, 812.
[4] J. Fang, H. Nakamura, H. Maeda, *Adv. Drug Delivery Rev.* **2011**, *63*, 136.
[5] a) M. A. Moses, H. Brem, R. Langer, *Cancer Cell* **2003**, *4*, 337; b) T. Minko, S. Dharap, R. Pakunlu, Y. Wang, *Curr. Drug Targets* **2004**, *5*, 389.
[6] G. Mikhaylov, U. Mikac, A. A. Magaeva, V. I. Itin, E. P. Naiden, I. Psakhye, L. Babes, T. Reinheckel, C. Peters, R. Zeiser, *Nat. Nanotechnol.* **2011**, *6*, 594.
[7] a) G. Von Maltzahn, J.-H. Park, K. Y. Lin, N. Singh, C. Schwöppe, R. Mesters, W. E. Berdel, E. Ruoslahti, M. J. Sailor, S. N. Bhatia, *Nat. Mater.* **2011**, *10*, 545; b) Z. Gao, H. D. Fain, N. Rapoport, *Mol.*

Pharma. **2004**, *1*, 317; c) N. Rapoport, D. Christensen, H. Fain, L. Barrows, Z. Gao, *Ultrasonics* **2004**, *42*, 943; d) H. Yan, C. Teh, S. Sreejith, L. Zhu, A. Kwok, W. Fang, X. Ma, K. T. Nguyen, V. Korzh, Y. Zhao, *Angew. Chem. Int. Ed.* **2012**, *51*, 8373.

[8] a) Y. Namiki, T. Namiki, H. Yoshida, Y. Ishii, A. Tsubota, S. Koido, K. Nariai, M. Mitsunaga, S. Yanagisawa, H. Kashiwagi, *Nat. Nanotechnol.* **2009**, *4*, 598; b) E. I. Galanzha, E. V. Shashkov, T. Kelly, J.-W. Kim, L. Yang, V. P. Zharov, *Nat. Nanotechnol.* **2009**, *4*, 855; c) N. L. Rosi, C. A. Mirkin, *Chem. Rev.* **2005**, *105*, 1547; d) L. Cheng, K. Yang, Y. Li, X. Zeng, M. Shao, S.-T. Lee, Z. Liu, *Biomaterials* **2012**, *33*, 2215; e) P. Huang, Z. Li, J. Lin, D. Yang, G. Gao, C. Xu, L. Bao, C. Zhang, K. Wang, H. Song, H. Hu, D. Cui, *Biomaterials* **2011**, *32*, 3447; f) F. Zhang, G. B. Braun, A. Pallaoro, Y. Zhang, Y. Shi, D. Cui, M. Moskovits, D. Zhao, G. D. Stucky, *Nano Lett.* **2011**, *12*, 61.

[9] a) Z. Medarova, W. Pham, C. Farrar, V. Petkova, A. Moore, *Nat. Med.* **2007**, *13*, 372; b) J.-H. Lee, Y.-M. Huh, Y.-w. Jun, J.-w. Seo, J.-t. Jang, H.-T. Song, S. Kim, E.-J. Cho, H.-G. Yoon, J.-S. Suh, *Nat. Med.* **2006**, *13*, 95.

[10] a) A. De La Zerda, C. Zavaleta, S. Keren, S. Vaithilingam, S. Bodapati, Z. Liu, J. Levi, B. R. Smith, T.-J. Ma, O. Oralkan, *Nature Nanotechnol.* **2008**, *3*, 557; b) M. F. Kircher, A. de la Zerda, J. V. Jokerst, C. L. Zavaleta, P. J. Kempen, E. Mittra, K. Pitter, R. Huang, C. Campos, F. Habte, *Nat. Med.* **2012**, *18*, 829; c) H. F. Zhang, K. Maslov, G. Stoica, L. V. Wang, *Nat. Biotechnol.* **2006**, *24*, 848; d) L. V. Wang, *Nat. Photonics* **2009**, *3*, 503.

[11] A. de la Zerda, S. Bodapati, R. Teed, S. n. Y. May, S. M. Tabakman, Z. Liu, B. T. Khuri-Yakub, X. Chen, H. Dai, S. S. Gambhir, *ACS Nano* **2012**, *6*, 4694.

[12] a) K. Wilson, K. Homan, S. Emelianov, *Nat. Commun.* **2012**, *3*, 618; b) S. Mallidi, T. Larson, J. Tam, P. P. Joshi, A. Karpiouk, K. Sokolov, S. Emelianov, *Nano Lett.* **2009**, *9*, 2825.

[13] a) S. Xuan, F. Wang, Y.-X. J. Wang, C. Y. Jimmy, K. C.-F. Leung, *J. Mater. Chem.* **2010**, *20*, 5086; b) S. Xuan, F. Wang, J. M. Lai, K. W. Sham, Y.-X. J. Wang, S.-F. Lee, J. C. Yu, C. H. Cheng, K. C.-F. Leung, *ACS Appl. Mater. Interfaces* **2011**, *3*, 237.

[14] M. D. Shultz, J. U. Reveles, S. N. Khanna, E. E. Carpenter, *J. Am. Chem. Soc.* **2007**, *129*, 2482.

[15] H. Xing, W. Bu, S. Zhang, X. Zheng, M. Li, F. Chen, Q. He, L. Zhou, W. Peng, Y. Hua, *Biomaterials* **2012**, *33*, 1079.

[16] a) H. Zhang, Y. Li, I. A. Ivanov, Y. Qu, Y. Huang, X. Duan, *Angew. Chem.* **2010**, *122*, 2927; b) L. Cheng, K. Yang, Y. Li, J. Chen, C. Wang, M. Shao, S. T. Lee, Z. Liu, *Angew. Chem.* **2011**, *123*, 7523.

[17] a) L. H. Reddy, J. L. Arias, J. Nicolas, P. Couvreur, *Chem. Rev.* **2012**, *112*, 5818; b) M. Mahmoudi, H. Hofmann, B. Rothen-Rutishauser, A. Petri-Fink, *Chem. Rev.* **2011**, *112*, 2323; c) B. Szalay, E. Tátrai, G. Nyírő, T. Vezér, G. Dura, *J. Appl. Toxicol.* **2012**, *32*, 446.

[18] N. Khlebtsov, L. Dykman, *Chem. Soc. Rev.* **2011**, *40*, 1647.

[19] E. Boisselier, D. Astruc, *Chem. Soc. Rev.* **2009**, *38*, 1759.

[20] a) W. Cai, X. Chen, *J. Nucl. Med.* **2008**, *49*, 113S; b) W. Cai, X. Chen, *Small* **2007**, *3*, 1840.

[21] a) Y.-S. Chen, W. Frey, S. Kim, P. Kruizinga, K. Homan, S. Emelianov, *Nano Lett.* **2011**, *11*, 348; b) C. Kim, E. C. Cho, J. Chen, K. H. Song, L. Au, C. Favazza, Q. Zhang, C. M. Cobley, F. Gao, Y. Xia, *ACS Nano* **2010**, *4*, 4559.

[22] C. Wang, H. Tao, L. Cheng, Z. Liu, *Biomaterials* **2011**, *32*, 6145.

[23] V. Torchilin, *Adv. Drug Delivery Rev.* **2011**, *63*, 131.

[24] J. Chen, D. Wang, J. Xi, L. Au, A. Siekkinen, A. Warsen, Z.-Y. Li, H. Zhang, Y. Xia, X. Li, *Nano Lett.* **2007**, *7*, 1318.

[25] a) E. Alphandery, S. Faure, O. Seksek, F. o. Guyot, I. n. Chebbi, *ACS Nano* **2011**, *5*, 6279; b) I. Hilger, W. Andrä, R. Hergt, R. Hiergeist, H. Schubert, W. A. Kaiser, *Radiology* **2001**, *218*, 570; c) S. Mornet, S. Vasseur, F. Grasset, E. Duguet, *J. Mater. Chem.* **2004**, *14*, 2161.

[26] a) X. Liu, H. Tao, K. Yang, S. Zhang, S.-T. Lee, Z. Liu, *Biomaterials* **2011**, *32*, 144; b) H. K. Moon, S. H. Lee, H. C. Choi, *ACS Nano* **2009**, *3*, 3707; c) K. Yang, S. Zhang, G. Zhang, X. Sun, S.-T. Lee, Z. Liu, *Nano Lett.* **2010**, *10*, 3318; d) Q. Xiao, X. Zheng, W. Bu, W. Ge, S. Zhang, F. Chen, H. Xing, Q. Ren, W. Fan, K. Zhao, *J. Am. Chem. Soc.* **2013**, *135*, 13041.

[27] a) S. A. Ermilov, T. Khamapirad, A. Conjusteau, M. H. Leonard, R. Lacewell, K. Mehta, T. Miller, A. A. Oraevsky, *J. Biomed. Opt.* **2009**, *14*, 024007; b) S. Manohar, S. E. Vaartjes, J. C. Hespen, J. M. Klaase, F. M. Engh, W. Steenbergen, T. G. Leeuwen, *Opt. Express* **2007**, *15*, 12277; c) L. V. Wang, S. Hu, *Science* **2012**, *335*, 1458.

[28] a) M. S. Yavuz, Y. Cheng, J. Chen, C. M. Cobley, Q. Zhang, M. Rycenga, J. Xie, C. Kim, K. H. Song, A. G. Schwartz, *Nat. Mater.* **2009**, *8*, 935; b) H. Liu, D. Chen, L. Li, T. Liu, L. Tan, X. Wu, F. Tang, *Angew. Chem.* **2011**, *123*, 921; c) G. von Maltzahn, J.-H. Park, A. Agrawal, N. K. Bandaru, S. K. Das, M. J. Sailor, S. N. Bhatia, *Cancer Res.* **2009**, *69*, 3892.